Supporting Information

A Universal Size-Controllable Top-Down Synthesis of Nanomaterials via Electrospray

Jun Xie [abc], Mingbo Xie [abc], Yeqiu Zhao [abc], Wanyi Shen [abc], Jiashu Li [abc], Qingwei Wang [abc], Xu Yan [abc], Meiqing Shi [abc], and Liyuan Chai [abc] and Liyuan Zhang [*abcd]

a. School of Metallurgy and Environment, Central South University, Changsha, 410083, China.

b. Chinese National Engineering Research Center for Control & Treatment of Heavy Metal Pollution, Changsha 410083, China.

c. State Key Laboratory of Advanced Metallurgy for Non-ferrous Metals, Changsha 410083, China.

d. Jiangxi Silicon New Material Technology Co., Ltd., Jiangxi 334600, China.

* Corresponding author. E-mail: atomic_liyuan@yeah.net.

Text S1. Chemicals

Primary quartz powder (Crystalline SiO_2, 2.6 μm, 99.5%) was purchased from Lianyungang Donghai Colorful Mineral Products Co., Ltd. Diamond powder (Single crystal C, 1.2 μm, 99.5%) and elemental platinum powder (Pt, 2.2 μm, 99.9% metals basis) were purchased from Shanghai Aladdin Biochemical Technology Co., Ltd. Elemental gold powder (Au, 1-3 μm, 99.99% metals basis) was purchased from Shanghai Shaen chemical Co., Ltd. Sodium chloride (anhydrous NaCl, 99%), potassium chloride (anhydrous KCl, 99%), and ammonia (HPLC $NH_3 \cdot H_2O$, 25%) were purchased from Sigma-Aldrich Trading Co., Ltd.

Text S2. Build an electrospray device

The electrospray device includes a syringe pump, a nozzle mechanism, a high-voltage power supply, a receiver mechanism, and an auxiliary mechanism, as shown in Schematic Diagram 1. The syringe pump delivers liquid to the nozzle at a specified flow rate. The nozzle mechanism is made up of one or multiple needle nozzles connected in parallel, each with an inner diameter of 100 μm. The positive terminal of the high-voltage power supply connects directly to the nozzle, while the negative terminal links to the receiver. The receiver mechanism features a conductive copper sheet base and can be a clean silicon wafer, TEM ultra-thin carbon films, UV quartz glass, or a petri dish. The auxiliary mechanism includes a temperature control device and a box to prevent dust contamination.

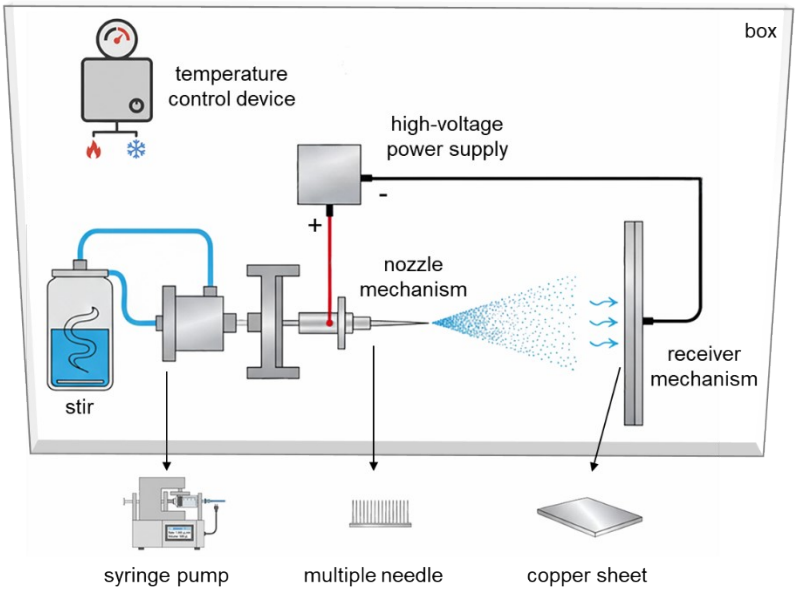

Schematic diagram 1. Electrospray device design connection diagram

Text S3. Experimental procedure

Raw material pre-treatment. Primary quartz powder is sieved through a 2500 mesh screen to remove large particles, then pre-treated as follows. Add 10 g sieved quartz powder to 100 ml ultrapure water, shake well, and sonicate for 20 minutes to promote dispersion. The ultrasonic suspension is allowed to settle for 20 minutes, after which the upper layer of liquid is poured off to remove particles smaller than 100 nm that may be in the feedstock. Add ultrapure water again to reach 100 ml, shake well, sonicate, let it precipitate, and pour off the top layer. Repeat these steps three times. At this point, SEM analysis shows that there are essentially no particles smaller than 100 nm remaining in the quartz powder. Diamond powder, elemental platinum powder, and elemental gold powder are processed using the same steps as described above.

Electrospray process. Add sodium chloride or potassium chloride, or ammonia to ultrapure water to adjust the conductivity to the target value and use it as the electrospray solvent. Add the pre-treated feedstock to the electrospray solvent to prepare the electrospray suspension. The suspension, with a solid concentration of 0.1-5 mg/ml, is fed into 12 parallel needles by a syringe pump at a flow rate of 4.8-96.0 ml/h. At this point, the flow rate per needle is 0.4-8.0 ml/h. Apply a positive voltage of 9-20 kV to the nozzle mechanism, with a distance of 2.0-3.0 cm between the needle tips and the substrates. The following materials are placed on a conductive copper base to form the receiver mechanism: a clean silicon wafer for SEM characterization, ultrathin carbon films for TEM characterization, UV quartz glass for Raman characterization, and petri dishes to collect the electrospray solutions. The temperature control device maintains an ambient temperature of 70°C during electrospray.

Text S4. Materials characterization

The scanning electron microscopy (SEM) observation of samples was conducted using a JEOL Model JSM-7610 FPlus. The transmission electron microscopy (TEM) observation of samples was carried out with a JEOL JEM-F 200. The energy-dispersive X-ray spectrometer (EDS) testing was performed using ULTIM MAX 40, Oxford. The X-ray diffraction (XRD) patterns were obtained with a Rigaku D/Max 2500 PC diffractometer using CuKα radiation (γ = 0.15418 nm) at room temperature, with the voltage and current set to 40 kV and 40 mA. X-ray photoelectron spectroscopy (XPS) spectra were recorded on a Thermo Scientific K-Alpha spectrometer. Fourier transform infrared (FTIR) spectra were collected using a Bruker Tensor 27-FTIR spectrometer

with the KBr pellet method, in the range of 400-4000 cm^{-1}. Laser confocal Raman spectroscopy (Raman) was measured using a Renishaw Invia. Laser particle size analysis (LDPA) of the samples was performed with a Microtrac S3500. ImageJ and Nano Measurer software were employed to analyze the size distribution of the nanoparticles after electrospray. For particles exceeding 10 nm, the equal-area circle diameter served as the size metric, whereas for those under 10 nm, the diagonal line measurement was used.

Text S5. Sample preparation for characterization

The electrospray plume initially covers the clean silicon wafer, which is then dried with an infrared lamp for SEM testing. Similarly, it covers the ultra-thin carbon film, also dried with an infrared lamp, and used for TEM testing. The electrospray plume directly covers the amorphous silicate glass substrate, which is transparent to XRD. The substrate is dried using an infrared lamp before being tested by XRD. The electrospray plume directly covers the petri dish. When the suspension at a specific concentration is collected in the dish, it is freeze-dried to eliminate water, resulting in electrospray powder. This powder is then used for XPS and FTIR analysis. The electrospray plume directly covers the UV quartz glass substrate, which is transparent to Raman. The UV quartz glass substrate is dried with an infrared lamp before Raman analysis is conducted.

Text S6. Calculation of electrical stress during the electrospray process

The main forces in electrospray can be decomposed into tangential electrical stress and normal electrical stress.[1-3] The tangential and normal electrical stresses for different electrical conductivities were calculated. The study explored the relationship between these stresses and conductivity, as well as the correlation between product size and conductivity. Simplified the calculation of tangential electrical stress, as shown in Eqn (1-3).[4-6]

$$\tau_t = q_s E_t \tag{1}$$

$$q_s(\sigma^-) \approx A_1 \varepsilon^+ E_{apex} \frac{\sigma^-}{\sigma^- + \sigma_c} \tag{2}$$

$$E_t(\sigma^-) \approx A_2 E_{apex} \frac{1}{1 + \sigma^-/\sigma_{eq}} \tag{3}$$

In the equation, for the determined electrospray system, these values are constants: A_1 and A_2 are the geometric/angular coefficients of the Taylor cone, ε^+ is the dielectric constant of air, E_{apex} is the local electric field strength between the cones, σ_c is the charging limit conductivity, and σ_{eq} is the conductivity dominated by the equipotentialization or space charge.

Here, tangential electrical stress (τ_t) is the product of the interface free charge density (q_s) and the tangential electric field component at the interface (E_t). From the above Eqn (1-3), function $\tau_t(\sigma^-)$ and normalized $\tau_t'(\sigma^-)$ can be derived, as shown in Eqn (4-5).

$$\tau_t(\sigma^-) = A_1 A_2 \varepsilon^+ E_{apex}^2 \frac{\sigma^-}{\sigma^- + \sigma_c} \frac{1}{1 + \sigma^-/\sigma_{eq}} \tag{4}$$

$$\tau_t'(\sigma^-) \approx \frac{\sigma^-}{\sigma^- + \sigma_c} \frac{1}{1 + \sigma^-/\sigma_{eq}} \tag{5}$$

Simplified the calculation of normal electrical stress, as shown in Eqn (6-7).[7-10]

$$\tau_n = \frac{1}{2}\varepsilon^+ E_n^2 + \frac{1}{2}(\varepsilon^- - \varepsilon^+)E_t^2 \tag{6}$$

$$E_n = q_s/\varepsilon^+ \tag{7}$$

From the above Eqn (2, 3, 6, 7), function $\tau_n(\sigma^-)$ and normalized $\tau_n'(\sigma^-)$ can be derived, according to Eqn (8-9).

$$\tau_n(\sigma^-) = \frac{1}{2}\varepsilon^+ A_1^2 E_{apex}^2 \left(\frac{\sigma^-}{\sigma^- + \sigma_c}\right)^2 + \frac{1}{2}(\varepsilon^- - \varepsilon^+) A_2^2 E_{apex}^2 \left(\frac{1}{1 + \sigma^-/\sigma_{eq}}\right)^2 \tag{8}$$

$$\tau_n'(\sigma^-) \approx C\left(\frac{\sigma^-}{\sigma^- + \sigma_c}\right)^2 + \left(\frac{1}{1 + \sigma^-/\sigma_{eq}}\right)^2 \tag{9}$$

In the equation, $\tau_n(\sigma^-)$ and $\tau_n'(\sigma^-)$ are the normal electrical stresses prior to and following normalization, respectively; E_n and E_t are the normal and tangential electric field components at the interface; ε^- and ε^+ are the dielectric constants of water and air, respectively; q_s is the interface free charge density; and C is the normalization constant.

Fig. S6 presents the quantitative evolution of electrical stresses derived from electrohydrodynamic scaling laws (Eqns. S5-S9). Quantitative analysis reveals a distinct mechanism: as conductivity rises to 5.25×10^{-5} S/m, the tangential electrical stress increases sharply to a peak, mirroring the experimental formation of the smallest

particles (~1.1 nm). In contrast, the normal electrical stress reaches a plateau and ceases to change. This divergence confirms that size controllability is strictly governed by the modulation of tangential stress.

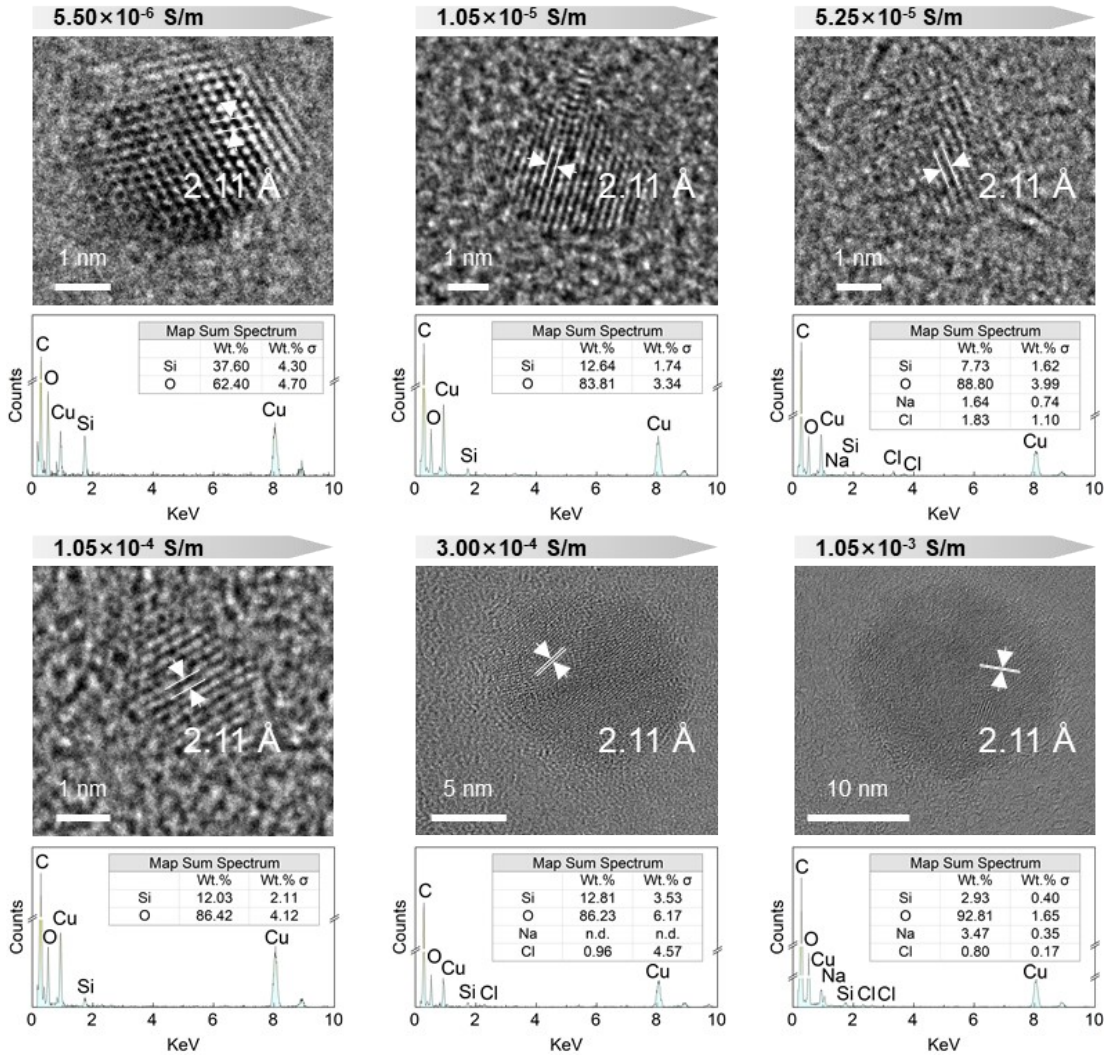

Fig. S1. The electrospray products from primary quartz suspension liquids with different conductivities are all quartz nanoparticles. The lattice spacing, as determined by HRTEM and EDS analysis, indicated that the nanoparticles were quartz. EDS detects Na and Cl because the solvent used to adjust the conductivity is NaCl.

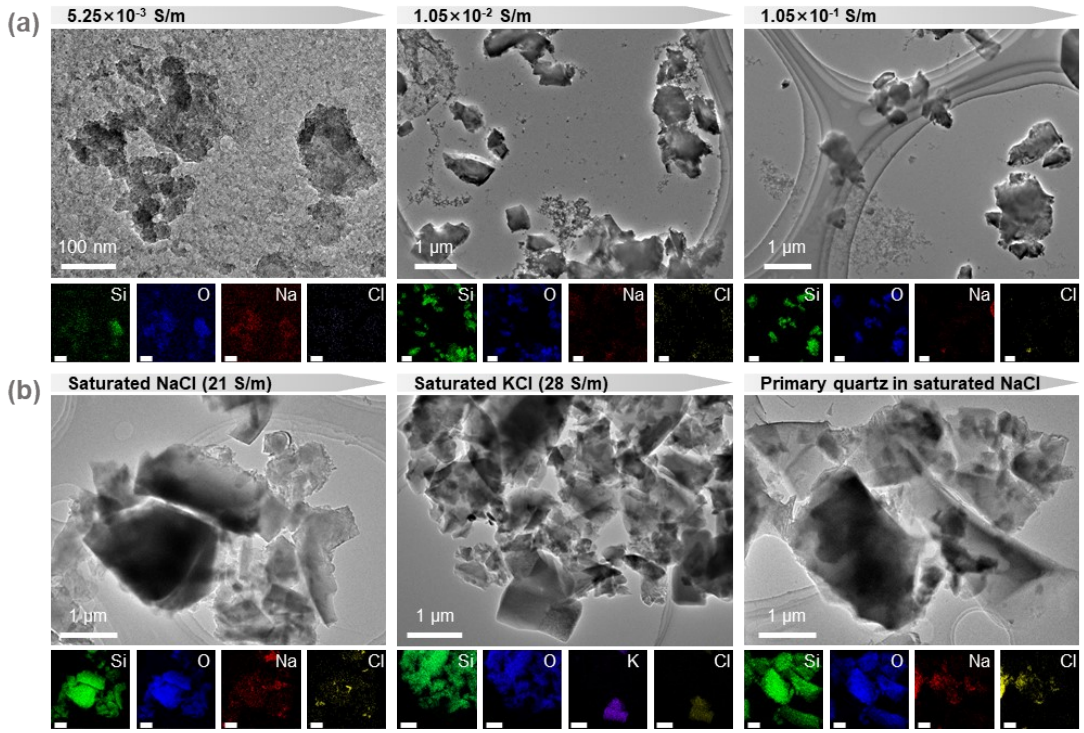

Fig. S2. Excessive conductivity causes the electrospray product to surpass 100 nm until fragmentation essentially vanishes. The quartz fragmentation caused by electrospray is independent of the solvent type and is solely dependent on conductivity. (a) When the solvent's conductivity is excessively high, the electrospray product size nearly matches that of the primary quartz. (b) The primary quartz size in saturated sodium chloride solution stays essentially the same before and after electrospray. When saturated potassium chloride replaces sodium chloride as the solvent, quartz fragmentation is still not observed.

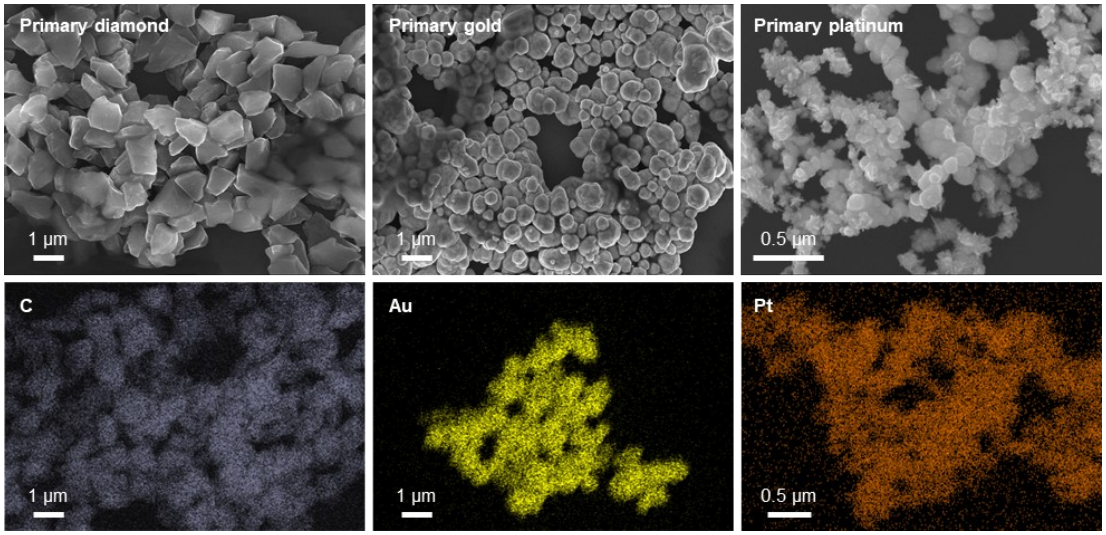

Fig. S3. Primary diamond, elemental gold, and elemental platinum are all measured in the micron range. EDS demonstrates that they are pure substances.

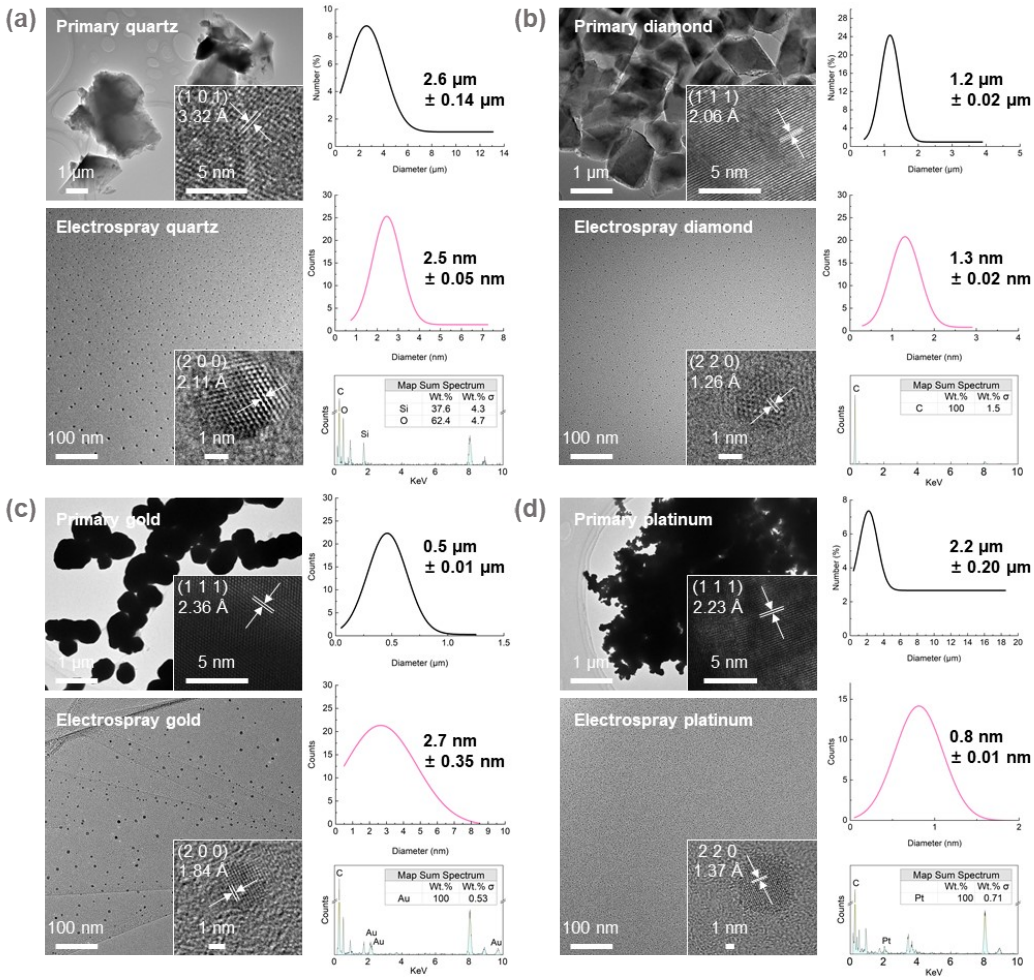

Fig. S4. Compared to the primary material on a micron scale, the electrospray products are clearly fragmented into nanoscale particles. Laser particle size analysis is used to measure the micron-scale dimensions of primary materials. Size statistics, reflecting a Gaussian distribution, help characterize the nanoscale size of electrospray products, as accurately measuring particles only a few nanometers in size remains a significant challenge in academia. The 100 nm scale bar shows numerous nanoparticles. Because of size effects, particles just a few nanometers in size are almost impossible to see visually on the micron scale bar. EDS characterizes the elemental makeup of electrospray products. (a) quartz. (b) diamond. (c) elemental gold. (d) elemental platinum.

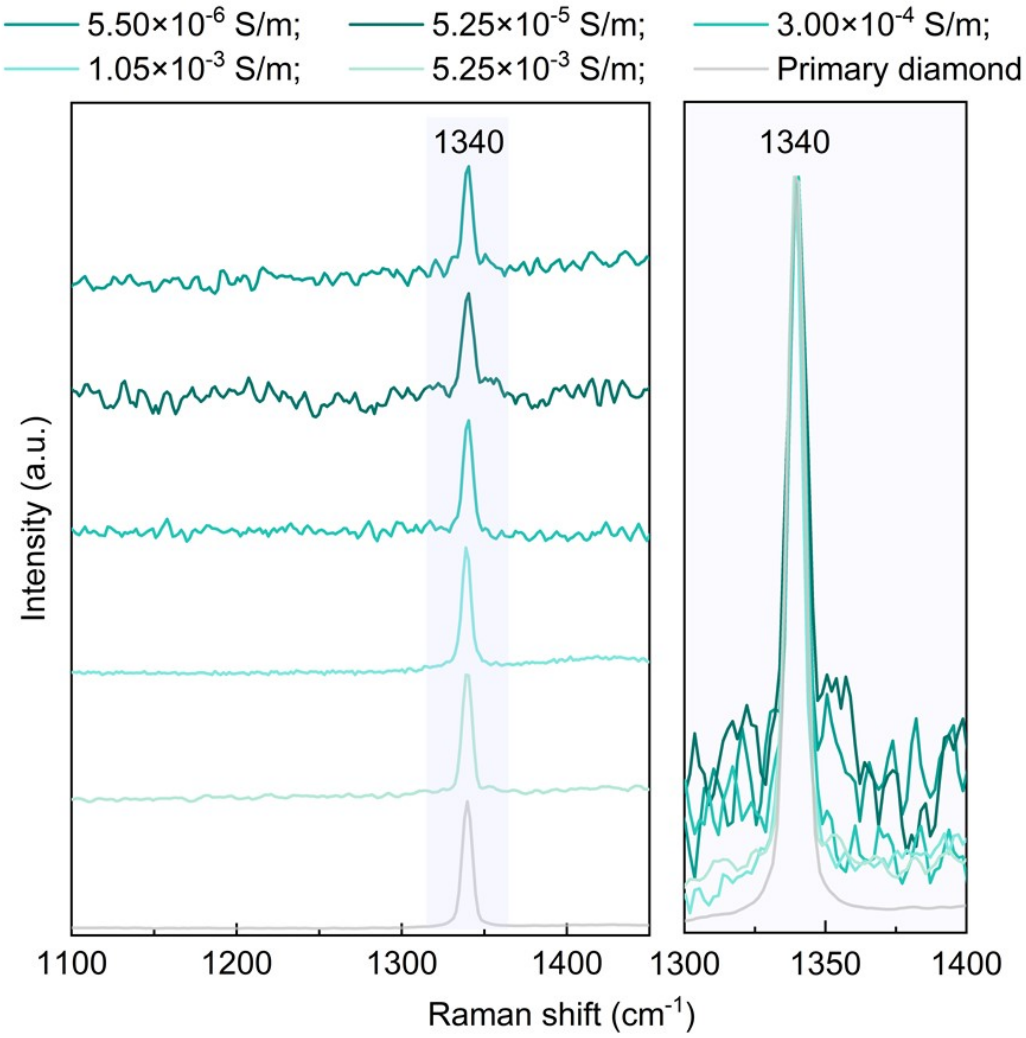

Fig. S5. The electrospray product has a much smaller crystal size than the primary diamond. Raman spectroscopy indicates that, among varying conductivities, the crystal sizes increase in the following order: 5.25×10^{-5} S/m, 5.50×10^{-6} S/m, 3.00×10^{-4} S/m, 1.05×10^{-3} S/m, and 5.25×10^{-3} S/m.

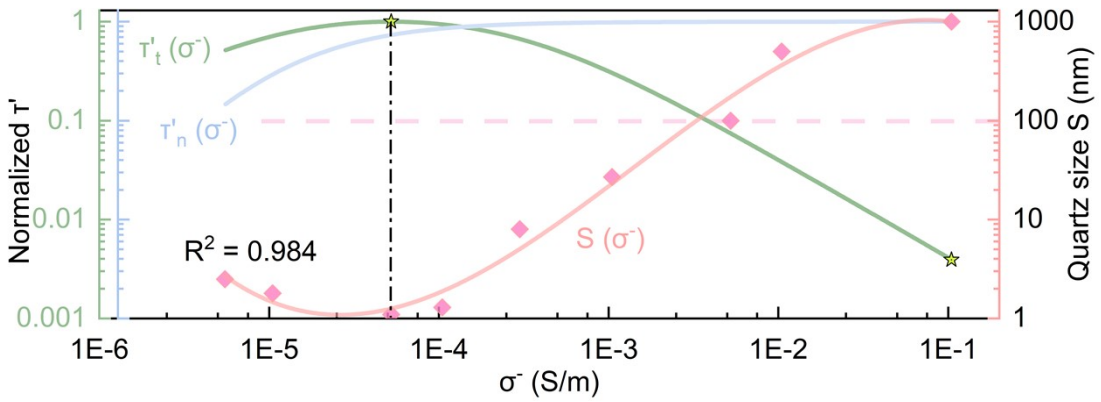

Fig. S6. Tangential electrical stress-conductivity and electrospray quartz size-conductivity are strongly negatively correlated, while normal electrical stress-conductivity shows no clear correlation with quartz size-conductivity. Normalized tangential electrical stress, normal electrical stress, and electrospray quartz size as a function of conductivity.

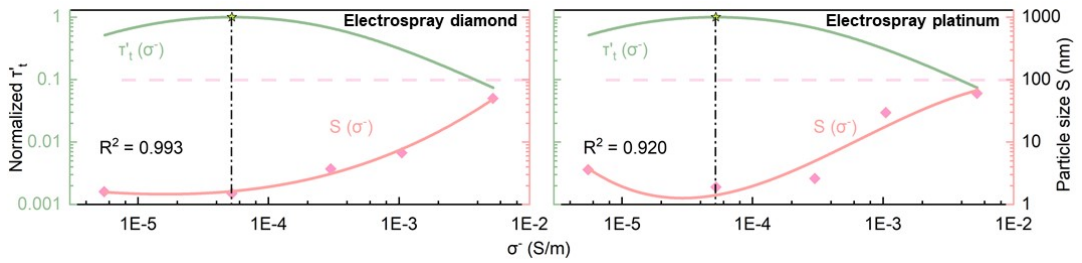

Fig. S7. Tangential electrical stress-conductivity and electrospray diamond (elemental platinum) size-conductivity are strongly negatively correlated. Normalized tangential electrical stress and electrospray diamond (elemental platinum) size as a function of conductivity.

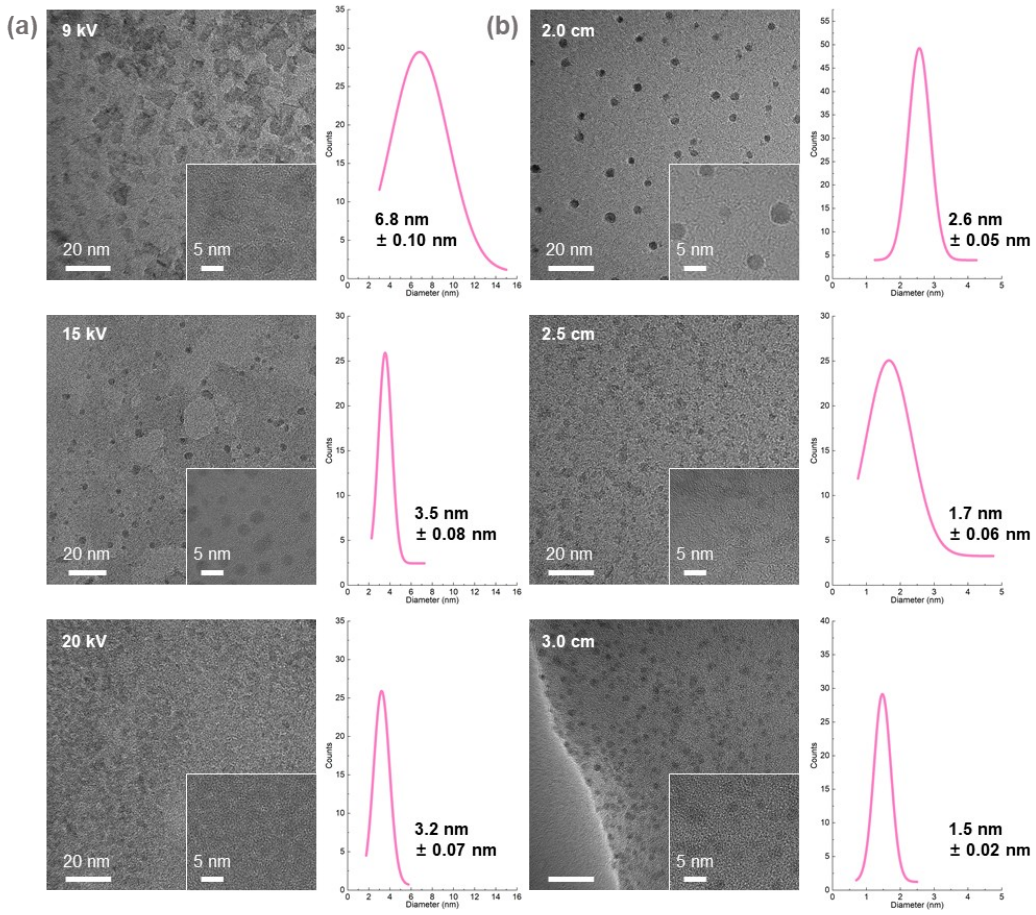

Fig. S8. The size of electrospray products decreases as either the applied potential or the working distance increases. (a) At an applied potential of 9-20 kV, the electrospray quartz size varies from 6.8 to 3.2 nm. (b) When the working distance is 2.0-3.0 cm, the electrospray quartz size ranges from 2.6 to 1.5 nm.

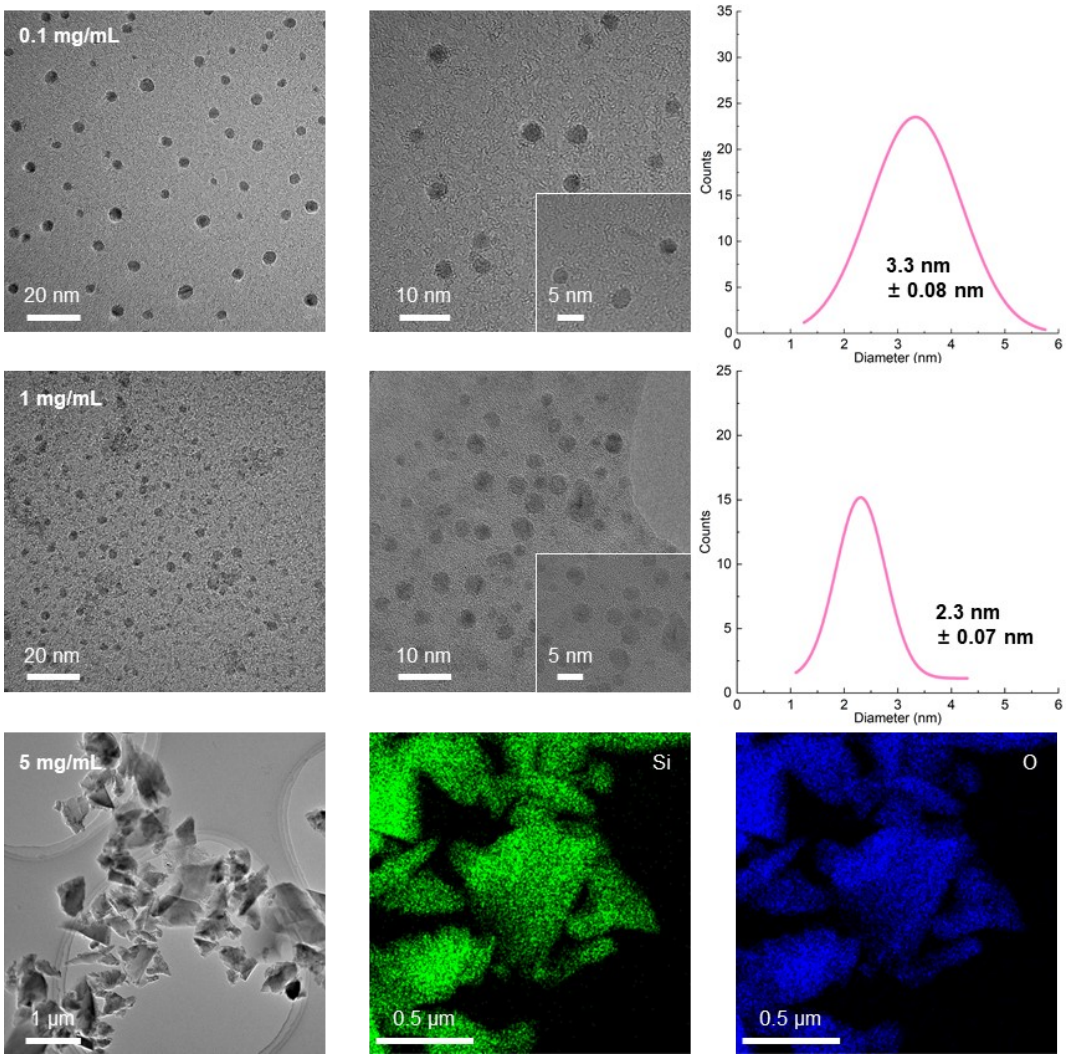

Fig. S9. When the concentration of solid particles becomes too high, quartz no longer fragments under electrospray. At solid concentrations of 0.1 mg/ml and 1 mg/ml, the sizes of the electrospray quartz are 3.3 nm and 2.3 nm, respectively. However, at a concentration of 5 mg/ml, the size of the electrospray quartz approaches that of primary quartz.

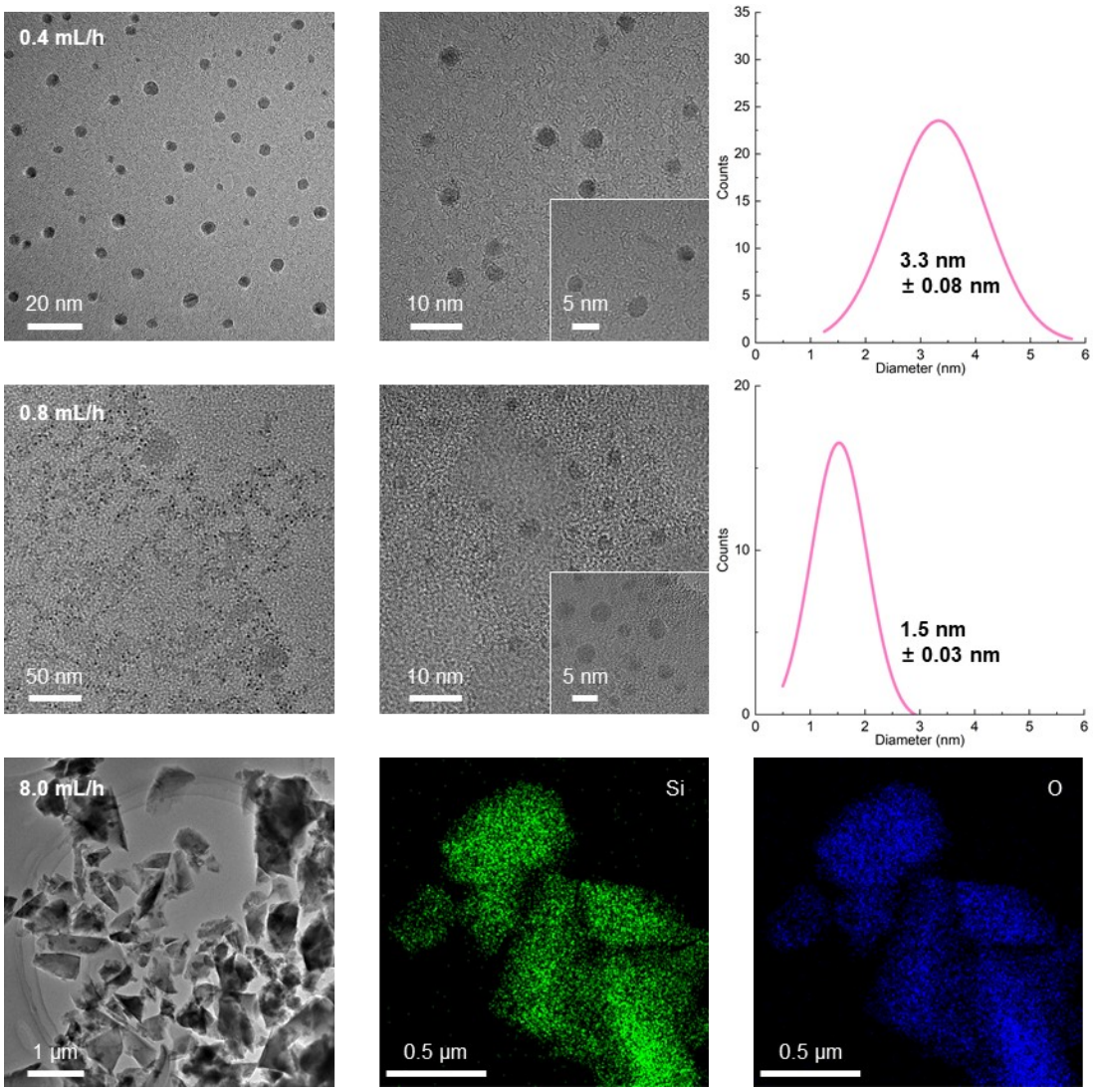

Fig. S10. When the flow rate of the single-needle solution is excessively high, the electrospray quartz's fragmentation phenomenon disappears. At flow rates of 0.4 ml/h and 0.8 ml/h for the single-needle solution, the electrospray quartz sizes are 3.3 nm and 1.5 nm, respectively. However, when the flow rate increases to 8.0 ml/h, the electrospray quartz size approaches that of primary quartz.

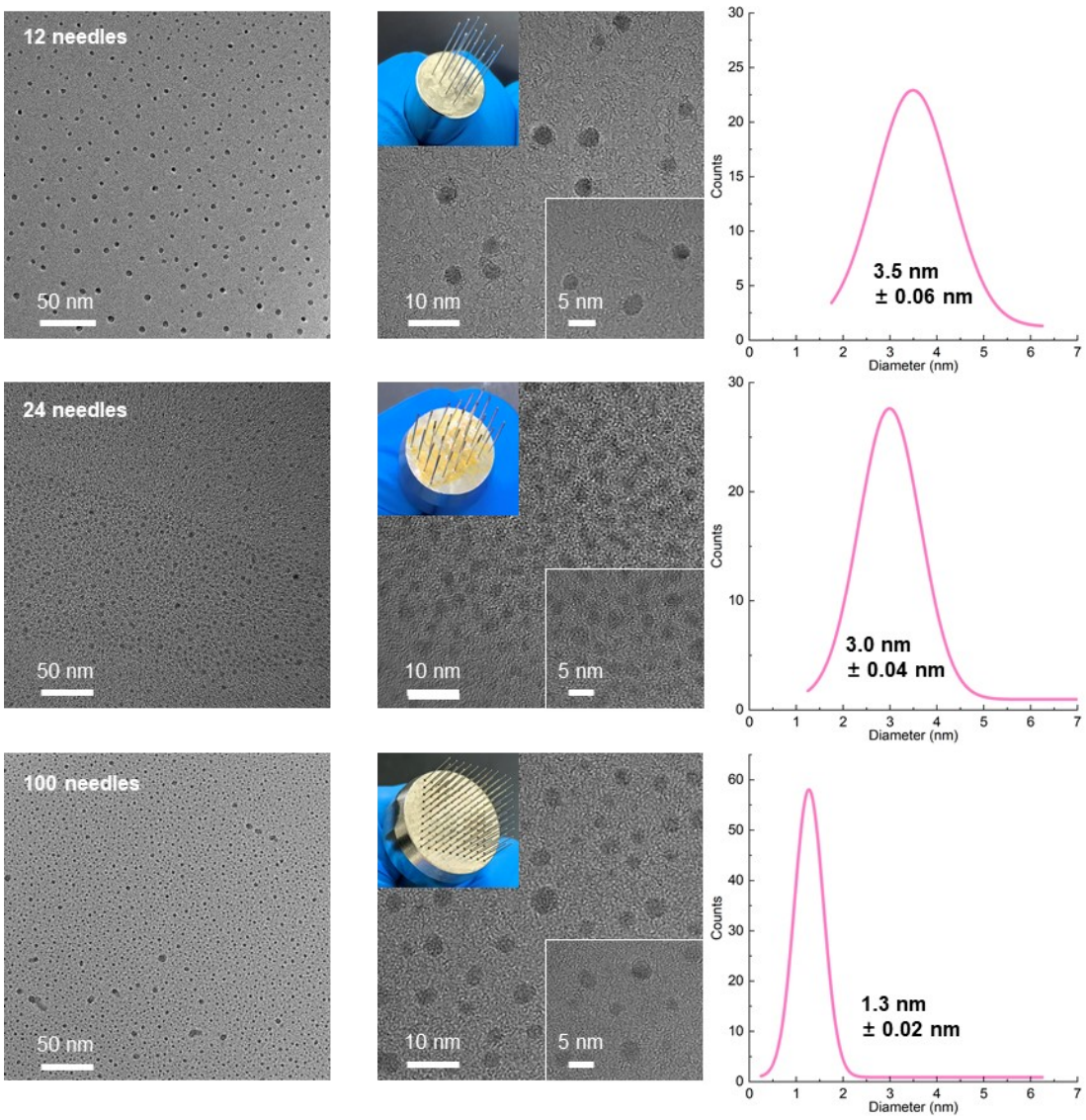

Fig. S11. By greatly increasing the number of parallel needles during electrospray, primary quartz can still be effectively fragmented into nano-quartz. When the number of parallel pins is 12, 24, and 100, the sizes of the electrospray quartz are 3.5 nm, 3.0 nm, and 1.3 nm, respectively.

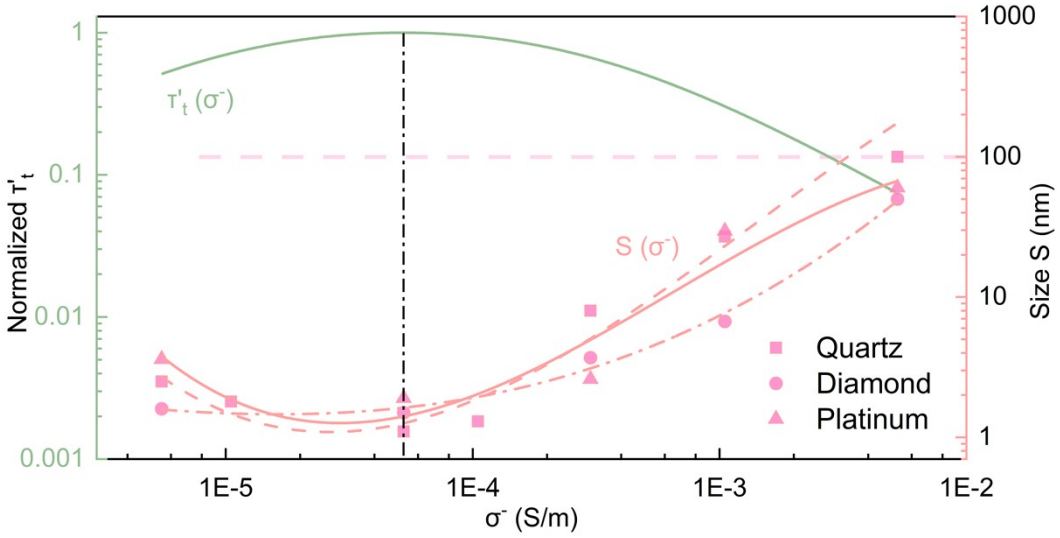

Fig. S12. Tangential electrical stress-conductivity and the size of electrospray materials-conductivity are strongly correlated. Normalized tangential electrical stress and electrospray materials (quartz, diamond, and platinum) size as a function of conductivity.

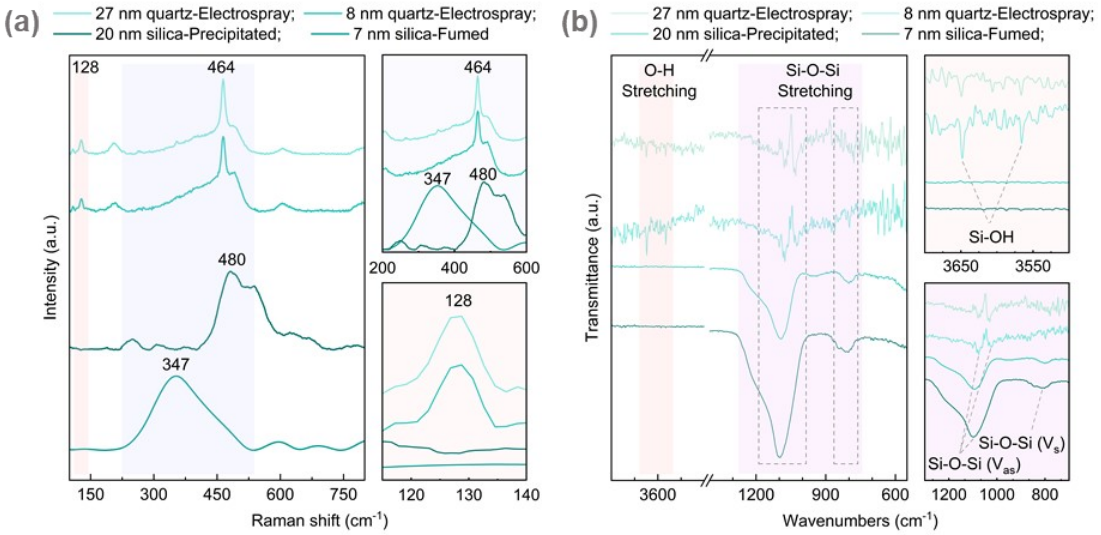

Fig. S13. Compared with those nanostructured materials of similar size, materials prepared by electrospray technology retain obvious crystal structures and have abundant Si-OH on the surface. (a) Raman spectroscopy and (b) infrared spectroscopy of electrospray quartz, precipitated silica, and fumed silica.

References

1. Z. Wang, Y. Chen, J. Xue, B. Li, J. Wang and Q. Dong, Electrospray modes of liquids in electrohydrodynamic atomization: A review, *Physics of Fluids*, 2024, **36**, 111304.
2. X. Li, J. Liang, J. Xiao, S. Su, L. Zhu, L. Sun, L. Gao, H. Wang, P. Yin, L. Chen and D. Wang, Substrate-Independent Electrohydrodynamic Jet Printing with Dual-Ring Electrostatic Focusing Structure, *Advanced Materials Technologies*, 2023, **8**, 2201842.
3. B. Aramide, A. Kothandaraman, M. Edirisinghe, S. N. Jayasinghe and Y. Ventikos, General Computational Methodology for Modeling Electrohydrodynamic Flows: Prediction and Optimization Capability for the Generation of Bubbles and Fibers, *Langmuir*, 2019, **35**, 10203-10212.
4. R. T. Collins, K. Sambath, M. T. Harris and O. A. Basaran, Universal scaling laws for the disintegration of electrified drops, *Proceedings of the National Academy of Sciences*, 2013, **110**, 4905-4910.
5. R. T. Collins, J. J. Jones, M. T. Harris and O. A. Basaran, Electrohydrodynamic tip streaming and emission of charged drops from liquid cones, *Nature Physics*, 2008, **4**, 149-154.
6. A. Yazdekhasti, A. Pishevar and A. Valipouri, Investigating the effect of electrical conductivity on electrospray modes, *Experimental Thermal and Fluid Science*, 2019, **100**, 328-336.
7. A. M. Gañán-Calvo, J. M. López-Herrera, M. A. Herrada, A. Ramos and J. M. Montanero, Review on the physics of electrospray: From electrokinetics to the operating conditions of single and coaxial Taylor cone-jets, and AC electrospray, *Journal of Aerosol Science*, 2018, **125**, 32-56.
8. R. Sengupta, L. M. Walker and A. S. Khair, The role of surface charge convection in the electrohydrodynamics and breakup ofprolate drops, *Journal of Fluid Mechanics*, 2017, **833**, 29-53.
9. N. Gawande, Y. S. Mayya and R. Thaokar, Jet and progeny formation in the Rayleigh breakup of a charged viscous drop, *Journal of Fluid Mechanics*, 2020, **884**, A31.
10. P. Biswas, R. M. Agarwal, B. Bhushan, A. Hens and G. Biswas, Interfacial hydrodynamics of electrosprays using leaky dielectric fluids, *Physics of Fluids*, 2025, **37**, 022149.